

AtomVision: A machine vision library for atomistic images

Kamal Choudhary^{ID},[†] Ramya Gurunathan^{ID},[†] Brian DeCost^{ID},[†] and Adam Biacchi^{ID}[‡]

[†]*Material Measurement Laboratory, National Institute of Standards and Technology, Gaithersburg, Maryland 20899, USA*

[‡]*Physical Measurement Laboratory, National Institute of Standards and Technology, Gaithersburg, Maryland 20899, USA*

E-mail:

Abstract

Computer vision techniques have immense potential for materials design applications. In this work, we introduce an integrated and general-purpose AtomVision library that can be used to generate, curate microscopy images (such as scanning tunneling microscopy and scanning transmission electron microscopy) datasets and apply a variety of machine learning techniques. To demonstrate the applicability of this library, we 1) generate and curate an atomistic image dataset of about 10000 materials with large structural and chemical diversity, 2) develop and compare convolutional and atomistic line graph neural network models to classify the Bravais lattices, 3) develop fully convolutional neural networks using U-Net architecture to pixelwise classify atom vs background, 4) use a generative adversarial network for super-resolution, 5) curate a natural language processing based image dataset using open-access arXiv dataset, and 6) integrate the computational framework with exper-

imental microscopy images for Rh, Fe₃O₄ and SnS systems. AtomVision library is available at the <https://github.com/usnistgov/atomvision>.

Introduction

Only a few experimental techniques allow a materials scientist to “see” the local atomic structure of a sample. Atomistic imaging techniques such as scanning tunneling microscopy (STM), atomic force microscopy (AFM), transmission electron microscopy (TEM) and their variants provide insights into the local atomic structure, defects and their dynamics, which are critically linked to the functionality and performance of the materials.¹ Due to rapid growth in computer-vision techniques,^{2,3} its application to atomic scale image data is natural. These data can be obtained from experimental as well as computational methods and recently their usage has become widespread.^{4–20} Nevertheless, an integrated library to capture, curate, generate datasets and apply data-analytics methods is still needed.

Such libraries can be useful for microscopy image tasks such as image classification,^{7,21–23} pixelwise learning (e.g., semantic segmentation),^{17,24–30} object/entity recognition, localization, super-resolution^{31–35} etc. The application of such libraries encompasses multiple science domains such as materials science, condensed matter physics, biology etc.^{5,8,36}

Computationally, there are several methods for simulating STM and scanning transmission electron microscopy (STEM) images. STM images can be computationally simulated using Bardeen,³⁷ Tersoff-Hamman³⁸ and Chen³⁹ methods. STM images can be either constant height or constant current based. For standard high angle annular dark field (HAADF) STEM, methods such as convolution, Bloch wave and multislice approximations^{40–43,43,44} can be used. The convolution approximation is one of the fastest ways to simulate STEM images. It is based on an incoherent linear image model that convolves the probe point-spread function with simple atomic potentials for the specimen and is usually used for thin films. Bloch wave and multislice methods are computationally heavy but are more generalizable.

Some of the major libraries (experimental and computational) based on microscopy images include ab initio Transmission Electron Microscopy (abTEM),⁴⁵ EXtraction, Separation, and Caption-based natural Language Annotation of IMages (EXCLAIM),²³ AtomAI,^{46, 47} Prismatic⁴⁸ and Quantitative TEM/STEM Simulations (QSTEM).⁴⁹ Deep learning techniques such as convolutional neural network (CNN) are commonly applied to atomistic image data. There have been several previous works on the application of deep-learning (DL) techniques⁵ to atomistic image data. In Ref²⁴ pixelwise DL was applied to detect atoms in simulated atomic-resolution TEM images of graphene. A neural network model was developed to detect the presence of atoms as well as predict its height. Ref²⁵ demonstrated atomistic defect recognition and tracking across sequences of atomic-resolution STEM images of WS₂. In ref²⁶ U-net architecture was used to detect vacancies and dopants in WSe₂ in STEM images with high model accuracy. In ref²⁷ DefectSegNet was developed to automatically identify defects in transmission and STEM images of steel including dislocations, precipitates, and voids. Ziatdinov *et al.* applied DL techniques to learn surface molecular structures.²⁹ In ref.,⁵⁰ artificial neural networks (ANN) were applied to classify eight types of 2D materials (in both monolayer and bilayer forms) and enumerate interface characteristics of 2D in-plane and vdW heterostructures. More details about previous works on atomistic imaging and machine learning techniques can be found elsewhere.^{5,8,36}

In this work, we present the AtomVision library, which can be used to generate a simulated STM/STEM dataset using several levels of approximation, as well as using natural language processing to collect images from literature and experiments. We also provide generalized scripts that can be used for a broad level of image machine learning tasks such as identifying five 2D-Bravais lattices,⁵¹ atomistic segmentation to distinguish between background and images and later applying convolutional neural network (CNN)/graph neural network (GNN) on the segmented images, and generative design of atomistic images using generative adversarial network (GAN) techniques. This library is a part of the NIST-JARVIS (Joint Automated Repository for Various Integrated Simulations) in-

frastructure⁵² for accelerated materials design using electronic structure, force-field, machine learning calculations and experiments. The atomvision library is publicly available at <https://github.com/usnistgov/atomvision>.

Although the methods discussed in the work are applied to STEM/STM images mainly, the deep-learning methods emphasized in the later sections can be applied to image datasets from other microscopy techniques also. The AtomVision package provides scripts to train various deep-learning models (e.g. U-net segmentation, classifier, autoencoder, generative adversarial network) on generic image datasets. The user simply needs to provide paths to the directories containing the training and test set of images. The user can also modify the default configuration settings used to train the model (e.g. batch size, number of epochs) as discussed later.

Moreover, the AtomVision package provides a large diversity in structure and chemistry of materials using both theoretical and experimental techniques in comparison to existing atomic image datasets with fixed chemistry such as graphene, FeTe etc. only. The application of graph neural networks (atomistic line graph neural network (ALIGNN)⁵³) and generative models (such as Super-Resolution Generative Adversarial Networks (SRGAN)) also provides promising aspects for atomistic image tasks which were not carried out previously to the best of our knowledge.

Methods

Dataset generation and curation

We use Tersoff-Hamann (TH) technique³⁸ to calculate the STM images of 2D materials. TH is a simple model of an s-wave STM tip.

$$n(r, E) = \sum_{\mu} |\psi(r)|^2 \delta(\epsilon_{\mu} - E) \tag{1}$$

$$\int_{E_F}^{E_F+eV} n(r, E) dE \quad (2)$$

In this approach, the tunneling current I , which depends on the tip position r and the applied voltage V , is proportional to the integrated local density of states (ILDOS). The ILDOS is calculated from the Kohn-sham eigenvectors, ψ_μ , and eigenvalues, ϵ_μ , where μ labels different states. E_F is the Fermi-energy. Different experiments will choose different applied voltages, but we concentrate on two values, 0.5 eV for positive bias and -0.5 eV for negative bias, which require integrating from E_F to $E_F \pm 0.5\text{eV}$. We choose 0.5 eV range for the sake of simplicity, and other values usually produce qualitatively similar images for metals or small gap semiconductors. However, simulations for other voltages should also be possible with the method and tools discussed in this work. This method is readily available in DFT software such as Vienna ab initio simulation package (VASP).^{54,55}

The STEM images^{40-43,43,44} were generated with the convolution approximation (based on fast Fourier transform based convolutions) following:

$$I(r) = R(r, Z) \otimes PSF(r) \quad (3)$$

where r is a 2D vector in the image plane, $I(r)$ is the image intensity,

$$R(r, Z) = \sum_i^N Z_i^{1.7} \delta(r - r_i) \quad (4)$$

$R(r, Z)$ is the transmission function of the N atoms at position r_i , and includes information about the atomic potential of the system given by Z_i , the atomic number of the atom. Rutherford scattering from the nuclear charge predicts a Z^2 dependence of the intensity, but the exponent is reduced by core electron screening, and depends on the detection collection angles. The power value of 1.7 is an approximate value that represents a compromise between these many factors. In previous works, the power values of 1.3-1.7⁵⁶ have also been used to

match experiments, however, for the sake of generality, we use 1.7 for all the systems. We note that for such STEM images only crystallographic coordinates and atom-type information are needed. The optimized geometries for the 2D materials were obtained from density functional theory calculations. We generate STEM images with an output size of 256x256 pixels for at least 2.5 nm x 2.5 nm size. The microscope point spread function (PSF) is modeled as a normalized Gaussian with a width of 0.5 Å. We use the 2D materials available in the JARVIS-DFT-2D,^{52,57} Computational 2D Materials Database (C2DB)⁵⁸ and 2DMatPedia⁵⁹ datasets, leading to 9150 systems with unique chemical compositions and structural spacegroup information.

For the natural language processing (NLP) related dataset, we use the open access arXiv dataset, which consists of 1.8 million articles starting from 1986 to 2020. We use ChemNLP⁶⁰ to extract chemistry information from the arXiv articles. We search for keywords such as STEM, STM, microscopy, HRTEM, scanning tunneling microscopy and scanning transmission electron microscopy in the abstract and figure captions of articles, and if the system has that info, we further find out if the article contains clear STM/STEM images to curate an image dataset. The figure caption parsing was carried out with the BeautifulSoup package.

Currently, the experimental STEM image dataset consists of images of nanoparticles. As an example experimental dataset we use TEM images of Iron oxide (Fe_3O_4), rhodium (Rh), and tin(II) sulfide (SnS) nanoparticles. In the future, we plan to expand this dataset to multiple systems, especially for the materials available in the JARVIS-DFT dataset. Iron oxide, rhodium, and tin(II) sulfide nanostructures were synthesized using previously reported solution strategies based on the thermal decomposition of elemental precursors. All syntheses were carried out under Ar using standard Schlenk techniques. Briefly, Fe_3O_4 spherical nanoparticles were synthesized by heating iron oleate in benzyl ether to 300 °C and then centrifugally washing twice before dispersing the collected product in hexanes.⁶¹ Rh triangular nanoplates were synthesized by heating $\text{RhCl}_3 \cdot x\text{H}_2\text{O}$ and 40,000 molecular weight poly(vinylpyrrolidone) in triethylene glycol to 135 °C before then centrifugally washing twice

and redispersing the product in ethanol.⁶² α -SnS micron-sized nanoribbons were synthesized by heating SnCl₂ and sulfur powder in oleylamine to 180 °C and then centrifugally washing twice before redispersing the product in toluene.⁶³ Transmission electron microscopy (TEM) images were collected using a Phillips EM-400 operating at an accelerating voltage of 120 kV and high-resolution TEM (HRTEM) images were obtained with an FEI Titan 80-300 operating at 300 kV. Samples were prepared by casting one drop of dilute nanomaterial solution onto 300-mesh Formvar and carbon-coated copper grids (Ted Pella). Please note that commercial products used in this work are identified to specify procedures. Such identification does not imply recommendation by National Institute of Standards and Technology (NIST).

Machine learning model

For the machine learning models, we primarily use the STEM dataset developed with the convolution approximation. We use several machine/deep learning approaches such as clustering, classification with convolution and graph convolution neural network, fully convolutional neural network using U-Net and generative adversarial network.⁴⁻²⁰ We provide a brief description of these methods, and more details can be found elsewhere.⁵

For clustering analysis, we use t-distributed stochastic neighbor embedding (t-SNE), which is a statistical method for visualizing high-dimensional data in a two- or three-dimensional map. The t-SNE plot was generated with the help of Scikit-learn library.⁶⁴ The images were flattened into a python numpy array and then their dimensionality was reduced using nonlinear t-SNE for visualization purposes. We also use the features of graphs based on the image samples for generating t-SNE plot details of which are given in the later section.

The pixelwise classification/semantic segmentation task was performed with segmentation-models-with-pytorch (SMP)⁶⁵ package using U-Net⁶⁶ pretrained model using Binary cross-entropy with logits loss (BCELogitLoss) function. All the supervised ML tasks used 75:25 training:testing of samples during training.

For the Bravais lattice classification task, we use DenseNet (Dense Convolutional Network)⁶⁷ with pre-trained model available in PyTorch.⁶⁸ We use a uniform size of 256x256 images for each material. We use Pytorch-Ignite library to setup the training run with Adam optimizer, 0.001 learning rate and negative log likelihood loss (NLLLoss) for 100 epochs.

After pixelwise classification, we convert the images into networkx and deep graph library graphs,⁶⁹ which are then used along with atomistic line graph neural network (ALIGNN)⁵³ for image classification tasks as well. We use maximum, minimum and mean intensity of blobs in the images as the node features, while a 4 Å cutoff is used to generate neighborlist and generate bond-angles of different nodes. We use a batch size of 32, learning rate of 0.001, AdamW optimizer, negative log likelihood loss (NLLLoss) and 50 epochs for ALIGNN training. We used the original hyperparameters of the ALIGNN model as used in ref.⁵³

We create a synthetic dataset of STEM images with low resolution (4 times lower resolution, i.e. 64x64 pixel images instead of 256x256) and high-resolution (as generated with convolution approximation) images and train a generative adversarial network (GAN) for image super-resolution (SR) using SR-GAN model.⁷⁰ In SR-GAN, we use the 4th layer of VGG19 (visual geometry group convolutional neural network that is 19 layers deep)⁷¹ as feature-extractor. We use a perpetual loss function during SR-GAN training, which is a combination of both adversarial loss and content loss. We train the model for 50 epochs, learning rate of 0.00008 and Adam optimizer during training.

Next, we analyze the reconstruction of image capabilities using an autoencoder model with PyTorch. We take the 256x256 image, and use an auto-encoder of dimension 1120. The decoding part of the model reconstructs the image in 256x256 size. We train the models for 200 epochs, with mean squared loss function, Adam optimizer, and a learning rate of 0.001.

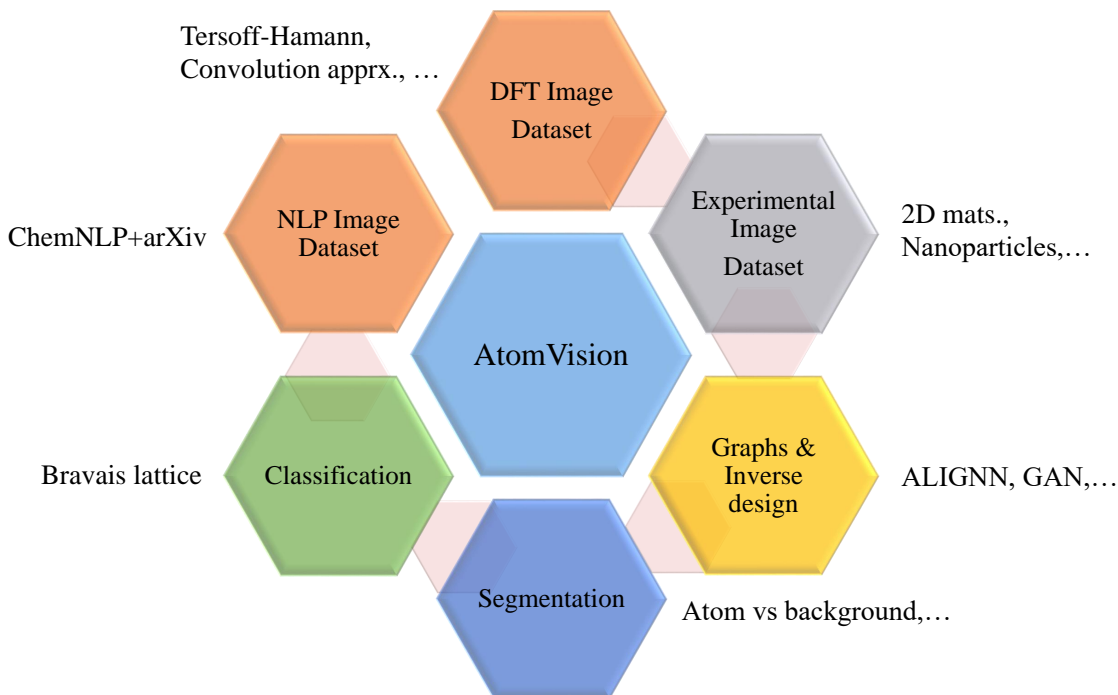


Figure 1: A Schematic overview of the AtomVision library. AtomVision presents an integrated library of dataset and AI/ML tools for atomistic images. The tool can be used for generating and curating microscopy dataset in a systematic manner as well as apply machine learning tools on the image dataset. This work aims to provide a software toolkit with integrated and diverse dataset and comprehensive AI/ML tools for expanding computer vision technique applications to atomistic images which include image quality resolution, image classification, segmentation and inverse design etc.

Results

A schematic overview of the AtomVision library is shown in Fig. 1. Usually, any image analytic technique application would require a large dataset. In AtomVision, the dataset can be obtained from density functional theory, convolution approximation, natural language approximation, and experiments. For instance, STM images for 2D materials in both positive and negative biases was obtained from the Tersoff-Hamann approach as implemented in the JARVIS-Tools. The STM image database consists of 1400 images for 2D materials in the JARVIS-DFT dataset. Although the application has been carried out for 2D materials, it can be applied to other non-2D systems as well. The STEM image dataset for 2D materials was obtained with the convolution approximation for systems in JARVIS-DFT, C2DB and

2DMatPedia computational datasets. While STM techniques require charge densities and wavefunctions to obtain integrated DOS values, the STEM dataset using the convolution approximation can be directly obtained with atomic types and coordinates information only.

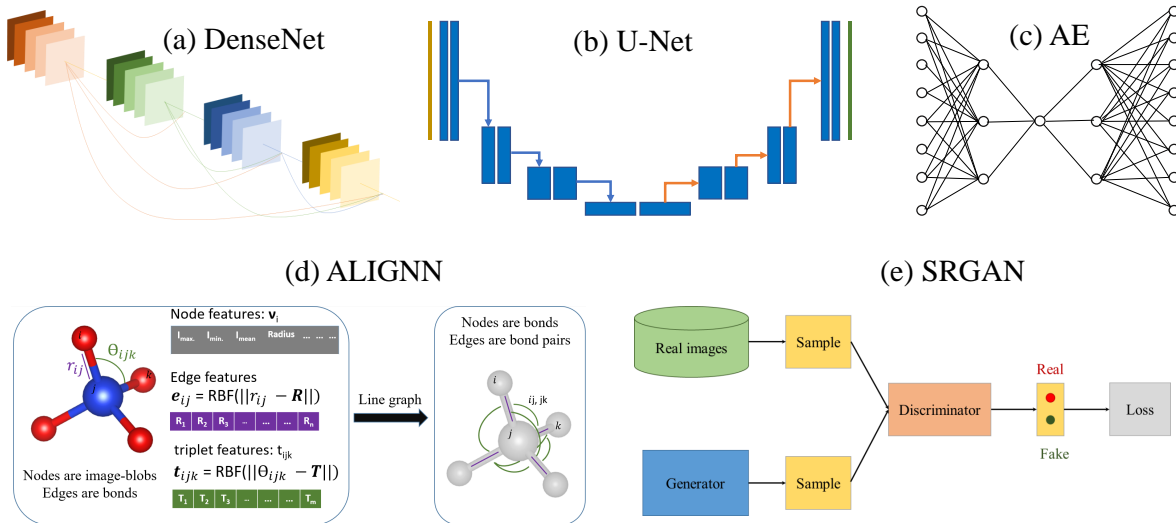


Figure 2: A few example machine learning architectures for images available in the AtomVision library. a) DenseNet is based on convolutional neural networks, b) U-net is a fully convolutional neural network, c) autoencoder, d) atomistic line graph neural network, e) super-resolution generative adversarial neural network.

We also show some of the machine learning architectures adopted in AtomVision in Fig. 2. These models are based on well-known deep learning models such as convolution neural network (CNN), graph neural network (GNN), and generative models such as auto-encoders (AE) and generative adversarial networks (GAN). The applications of these architectures and their performances are discussed in detail below.

Validation of dataset

We compare the STM and STEM simulated images of a few example 2D materials: graphene, FeTe and MoS₂, with experimental images in Fig. 3. The left panel (panels a,e,i) show

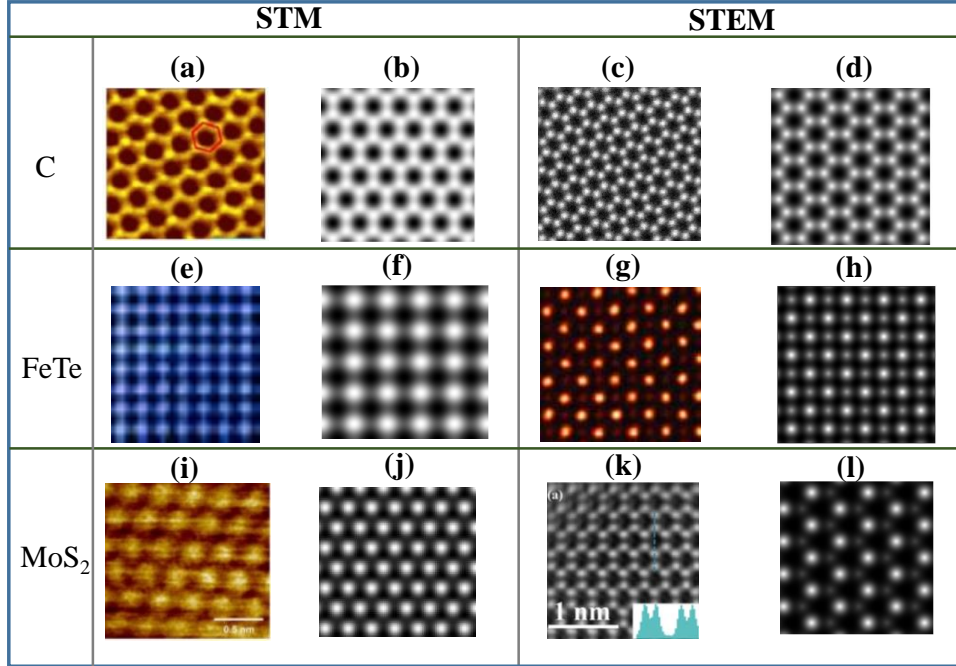


Figure 3: Comparison of our computational and previously reported experimental STM and STEM images for a few examples such as graphene, C (JVASP-667), FeTe (JVASP-6667), MoS₂ (JVASP-664). a) experimental STM image of graphene [Reproduced with permission from ref.⁷² Copyright 2019 American Physical Society], b) simulated STM image of graphene, c) experimental STEM image of graphene [Reproduced with permission from ref.⁷³ Copyright 2021, OLeary et al. Authors under Creative Commons Attribution 4.0 International License (CC BY 4.0)], d) simulated STEM image of graphene, e) experimental STEM image of FeTe [Reproduced with permission from ref.⁷⁴ Copyright 2015, Watashige et al. Authors under Creative Commons Attribution 4.0 International License (CC BY 4.0)], f) simulated STEM image of FeTe, g) experimental STEM image of FeTe [Reproduced with permission from ref.⁷⁵ Copyright 2021, Kang et al. Authors under Creative Commons Attribution 4.0 International License (CC BY 4.0)], h) simulated STEM image of FeTe, i) experimental STM image of MoS₂ [Reproduced with permission from ref.⁷⁶ Copyright 2016 AIP Publishing], j) simulated STM image of MoS₂, k) experimental STEM image of MoS₂ [Reproduced with permission from ref.⁷⁷ Copyright 2016 AIP Publishing], l) simulated STEM image of MoS₂.

experimental STM images, while DFT based images are shown in the next column (in panels b,f,j). Similarly, we show the experimental STEM images for graphene, FeTe, and MoS₂ in Fig, c,g,k and corresponding convolution approximation based images are shown in Fig. d,h,l. Clearly, we find excellent qualitative agreement between the simulated and experimental images. Furthermore, we note that theoretical image datasets are larger and can be generated in a very controlled way compared to experimental images. Hence, a

comparison of a few samples gives a qualitative idea that computer vision techniques applied to a theoretical image dataset should indicate similar confidence with respect to experiments.

Semantic Segmentation and Graph Generation

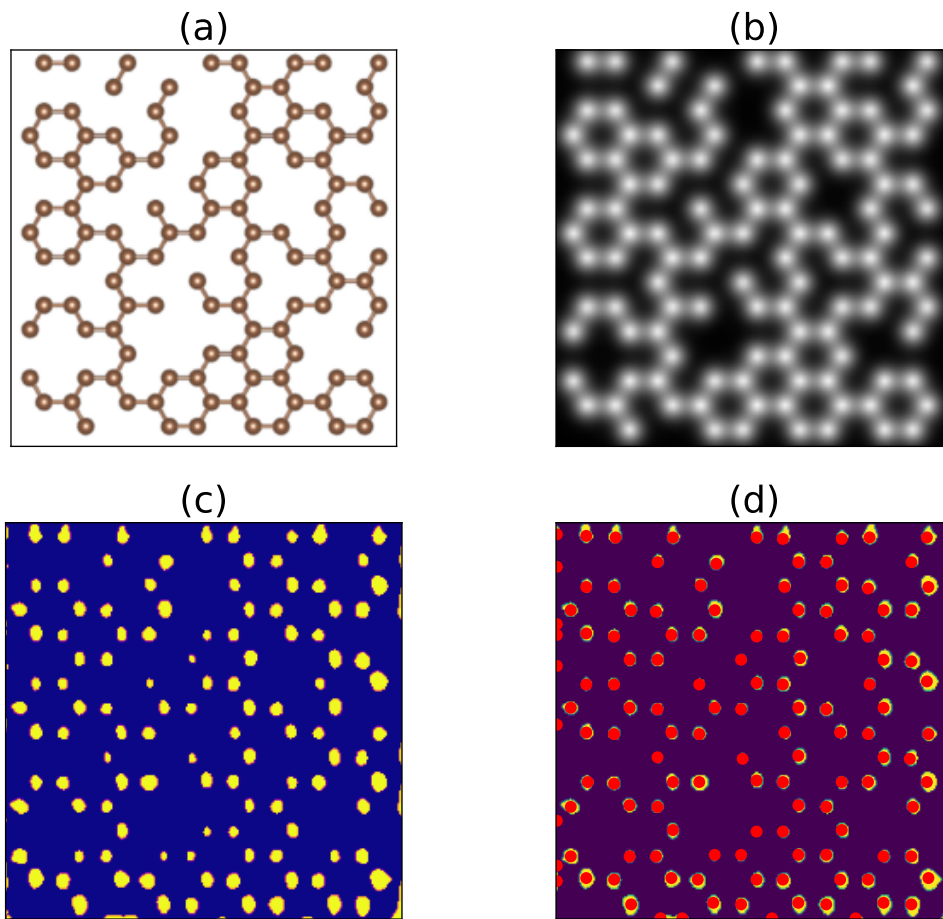


Figure 4: Application of semantic segmentation model to identify atoms and background from defective graphene system. a) Generate atomic structure for defective graphene (JVASP-667) with vacancies using JARVIS-Tools, b) STEM image for the atomic structure c) use the semantic segmentation model, d) blob detection algorithm to find the number of atoms.

A common first deep-learning image analysis task is to perform a pixelwise classification to differentiate bodies of interest in the image from the background. We use the U-Net model to perform atom vs. background classification tasks using the HAADF-STEM datasets. U-

net is a fully convolutional neural network with a U-shaped architecture consisting of a specific encoder-decoder scheme (as shown in Fig. 2). The encoder reduces the spatial dimensions in every layer and increases the channels. On the other hand, the decoder increases the spatial dimensions while reducing the channels. We use the pretrained U-Net model in the SMP library and fine tune with the HAADF-STEM dataset generated in this work for pixelwise classification of atom vs background classes. We find that high accuracy of 93.0 % for the pixelwise classification of atom vs. background task. As an application for this model, we first generate synthetic graphene HAADF-STEM images with vacancies and use the semantic segmentation model to localize the atoms in the image as shown in Fig. 4. We find that the model can accurately identify atom and background from the image. Later, using scikit-image⁷⁸ based blob detection we can find the number of atoms in the image. The blob detection algorithm identifies features in the image by fitting a Gaussian to the intensity profile, and the blob radius is related to the standard deviation. With scikit-image, we can also get various statistics of the blobs (atoms) such as the maximum, minimum, and mean intensities in the blob.

Once the atom positions are identified in the image, there is an opportunity to construct a non-Euclidean, undirected graph representation of their arrangement. The nodes of the graph come from the detected blobs (atoms) and are featurized by the blob features such as max intensity and radius. To determine the edges of the graph, which represent bond vectors between the atoms, a nearest neighbor search is performed using the k-d tree algorithm implemented in `scipy`. Finally, the linegraph is constructed using the `dgl` package on top of the original graph. The linegraph encodes bond vectors as the node features, while the edges represent triplets of atoms and encode bond angle cosines. The establishment of the graph and linegraph representations of the micrographs will allow us to apply graph neural networks for image analysis tasks.

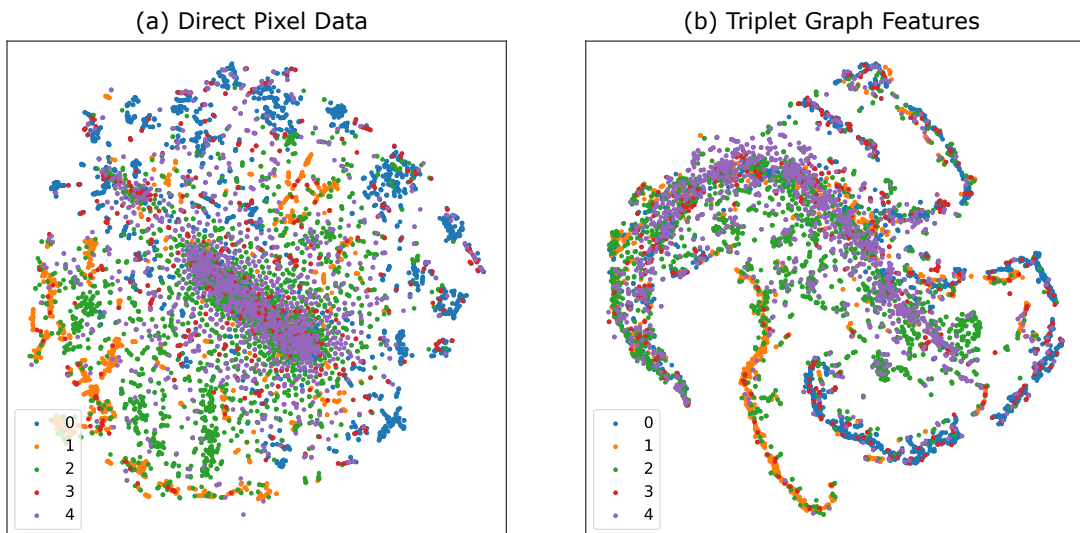


Figure 5: t-SNE visualization of the samples in the combined dataset including the JARVIS-DFT-2D and C2DB databases. In panel (a), the samples are featurized directly using the 256x256 pixel image intensity data. In contrast, in panel (b), the samples are featurized using their triplet (bond angle cosine) features in graph construction. The distribution of triplet features is expressed as a 200-bin histogram ranging from -1 to 1. Here, we denote hexagonal, square, rectangle, rhombus and parallelogram classes as 0,1,2,3,4 respectively. We observe clusters of individual classes in both t-SNE figures.

Clustering analysis

Prior to performing machine learning tasks, we applied clustering techniques and dimensionality reduction to visualize and understand the distribution of images in the synthetic dataset. We apply the t-SNE (t-distributed stochastic neighbor embedding) algorithm, which is commonly applied to visualize high-dimensional data such as our 256x256 pixel images by performing non-linear dimensionality reduction operations. The Euclidean distance between datapoints in a t-SNE plot relates to their similarity, however, these distances should only be interpreted qualitatively. Therefore, images which cluster together in the t-SNE plot will tend to be more similar in their featurization.

We first apply the t-SNE visualization directly to the simulated 256x256 pixel-based STEM image data for the 2D materials. These image array values for all the 2D materials in the dataset are converted into two-dimensions and are visualized in Fig. 5a. Each scatterpoint therefore represents an image in the dataset and is colored by the 2D Bravais lattice of the material in the image. From this visualization, it is clear that hexagonal class 0), square (class 1), and rectangle (class 2) systems segregate into islands in the pixel space, while the rhombus (class 3) and parallelogram (class 4) systems show greater overlap with other classes, suggesting more likely misclassifications.

We then perform a similar visualization for the features obtained through the graph generation process described in Section . As described previously, these graph features represent atom positions (nodes), bond vectors (edges), and bond angles (triplets of atoms) in the image. In Figure 5b, we use the t-SNE algorithm to visualize the dataset once again with the images now labelled using the set of graph triplet features, or the bond angle cosine values. Here, the list of bond angle features for each image is encoded in a 200-bin histogram before applying the t-SNE operation to investigate clustering. Once again, we find a noticeable separation of the hexagonal and square clusters, but a significant overlap between the hexagonal and rhombus classes as well as the rectangle and parallelogram classes, which may lead to misclassifications. Such analysis provides a visualization of large dimensional

data in a compact way to suggest that both image pixel values and graph features contain information about the Bravais lattices.

CNN Classifier

Now, we use a supervised classification technique to classify images into the five 2D Bravais lattices: hexagonal, square, rectangular, rhombus (rectangular centered), and oblique (parallelogram).⁵¹ We use a well-known computer vision model: DenseNet to perform this task. In a DenseNet architecture, each layer is connected to every other layer, hence the name is given as Densely Connected Convolutional Network. For L layers, there are $L(L+1)/2$ direct connections. For each layer, the feature maps of all the preceding layers are used as inputs, and its own feature maps are used as input for each subsequent layers. DenseNet was developed to improve the vanishing gradient issues in deep convolutional neural networks. We fine-tune the DenseNet model⁶⁷ for 5 Bravais lattice classes using the STEM image dataset. We find that DenseNet provided an accuracy of 83.0 %. We note that the baseline model for such classification task is $1/5 = 20$ %, so using machine vision techniques is clearly justified. In addition to the overall accuracy of the model, confusion matrix of the classification task provide details for individual class performance as shown in Fig. 6a. Here, we denote hexagonal, square, rectangle, rhombus and parallelogram classes as 0,1,2,3,4 respectively. We find that the trained model is highly accurate for hexagonal and square lattice but less accurate for rhombus and parallelogram classes, which can be attributed to less training data and higher complexity for these classes.

ALIGNN-based GNN classifier

In the previous section, an image classifier was trained directly on the pixelated images. Here, we instead convert the image data into a non-Euclidean graph, which infers the connectivity of the objects in the image, allowing the usage of a graph neural network. Graph neural networks have been widely applied in the field of materials science as they allow for the

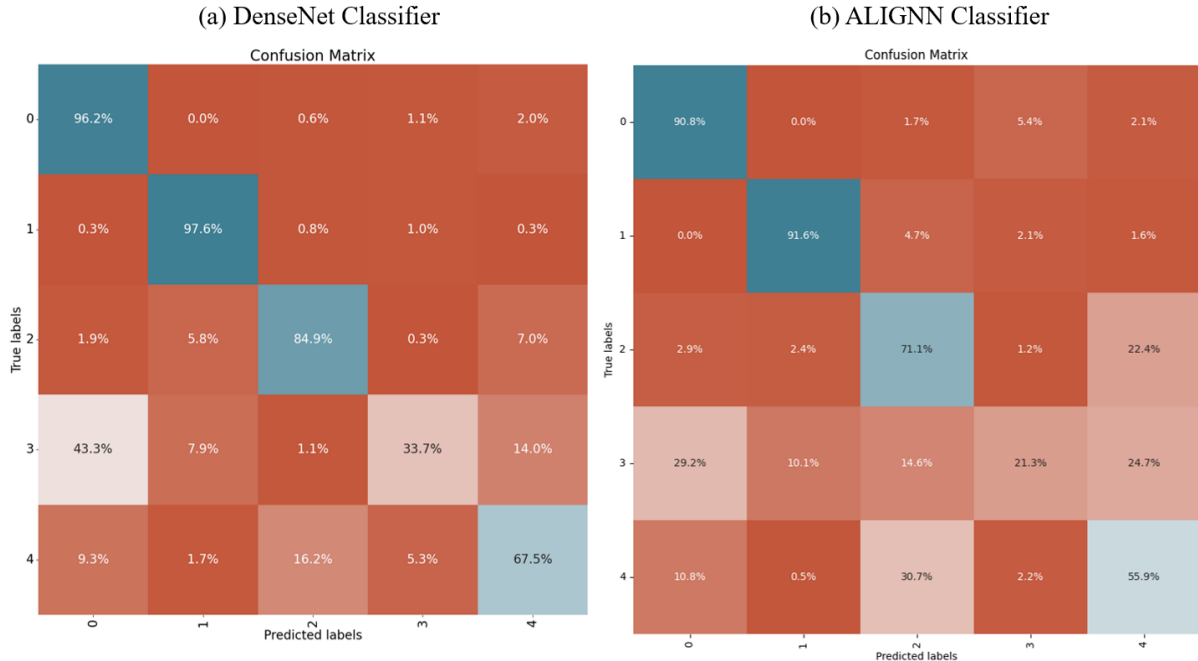


Figure 6: Confusion matrix for classifying STEM images into five Bravais lattices using a) convolution neural network based Densenet, b) graph neural network based ALIGNN models. Here, we denote hexagonal, square, rectangle, rhombus and parallelogram classes as 0,1,2,3,4 respectively.

structure of the material, along with composition-based features to be used in the prediction. Typically, graph neural networks are used to predict a material property from its structure, including both scalar quantities such as formation energy, bulk modulus, or band gap, or more recently, spectral quantities such as electron and phonon density-of-states or measured optical spectra (e.g. X-ray, infrared, Raman).⁵ To our knowledge, a graph neural network has not yet been applied to materials science image data, as it is in this work. The atomistic line graph neural network (ALIGNN)⁵³ was used, as it allows a hierarchy of structural features corresponding to single objects (i.e., atoms), pairs of objects (i.e., bond vectors), and pairs of bonds (i.e., bond angles). ALIGNN uses edge-gated graph convolution for updating nodes as well as edge features. One ALIGNN layer composes an edge-gated graph convolution on the bond graph with an edge-gated graph convolution on the line graph. The line graph convolution produces bond messages that are propagated to the atomistic graph, which further updates the bond features in combination with atom features.

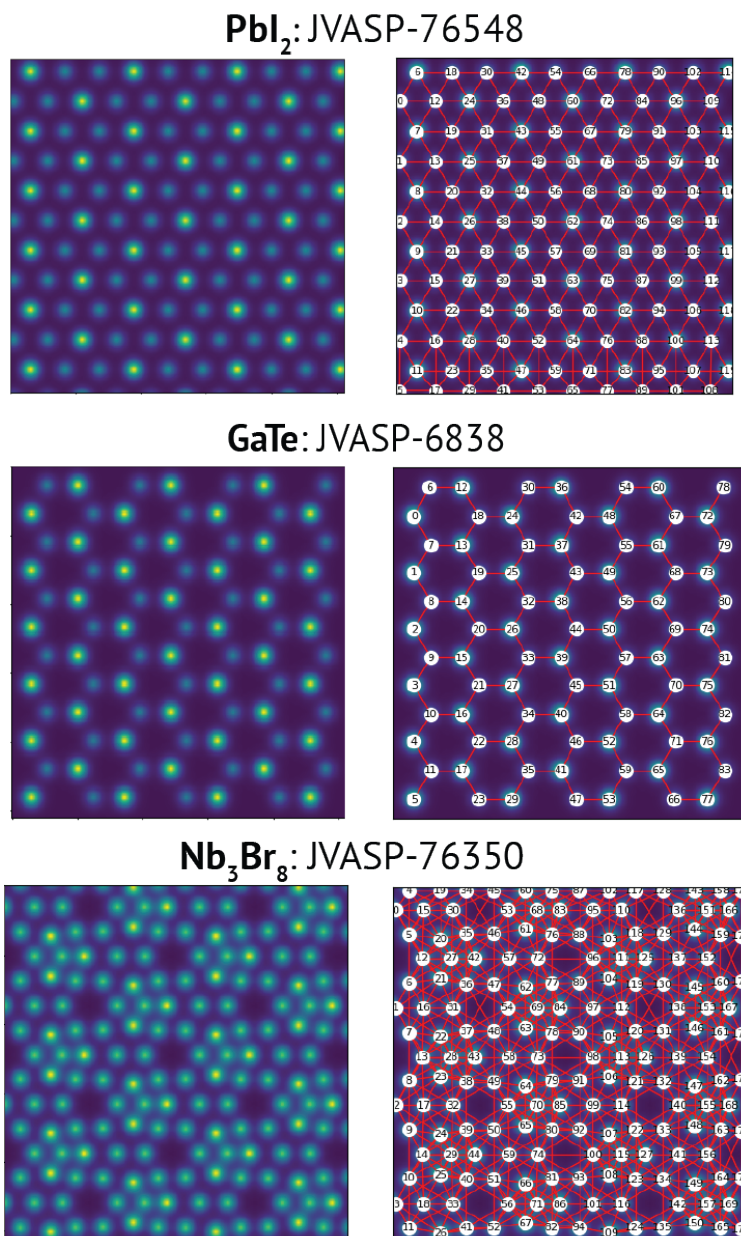


Figure 7: Computed STEM images (right) and overlaid graph construction (left) for three example materials in the hexagonal crystal system (class 0) and (001) orientation. Although the lattices are visually diverse, the DenseNet and ALIGNN crystal system classifiers correctly categorize over 90 % of the class 0 samples.

After the pixelwise classification, we can convert the data into graph that can capture non-Euclidean information of the images and can be used for advanced ML techniques such as the application of graph neural network. Examples of three systems with hexagonal symmetry (Pb_2I , GaTe and Nb_3Br_8) are shown in Fig. 7. After the graph conversion, we use the ALIGNN model for lattice classification and find a reasonable accuracy of 78%. Note that, unlike the original ALIGNN model which uses atomic attributes such as electronegativity as node features, we use the blob-statistics (such as maximum, minimum and mean intensities in a blob) as the node attributes. Therefore, knowledge of chemistry is not required to train and execute the model. The confusion matrix for the model is shown in Fig. 6b. Although, the GNN-based models do not beat CNN models such as DenseNet, the framework for applying GNNs on images could be a powerful alternative tool for futuristic materials design because GNN-based methods can incorporate additional relationships and parameters that are not strictly related to the appearance of the image. Additionally, from Fig. 6, we find that both the CNN and GNN models work well for hexagonal and square lattices but they are less accurate for rhombus lattices.

Autoencoders

Autoencoders (AE) are a special type of neural network especially suited for learning low-dimensional representations of high-dimensional data. We can think of autoencoders as being composed of two networks, an encoder and a decoder. The encoder learns a non-linear transformation from the original high-dimensional input space to a lower-dimensional latent space. A decoder learns a non-linear transformation that projects the latent vectors back into the original high-dimensional input space. We develop an auto-encoder to reduce the large pixel-dimension. Usually an image taken as 256×256 if flattened leads to 50176 (i.e., 256×256) dimension, which is quite high. According to the manifold hypothesis, the underlying structure of the data can be sufficiently described using only a few dimensions, and auto-encoders are well-known for such dimensionality reduction tasks. We take the

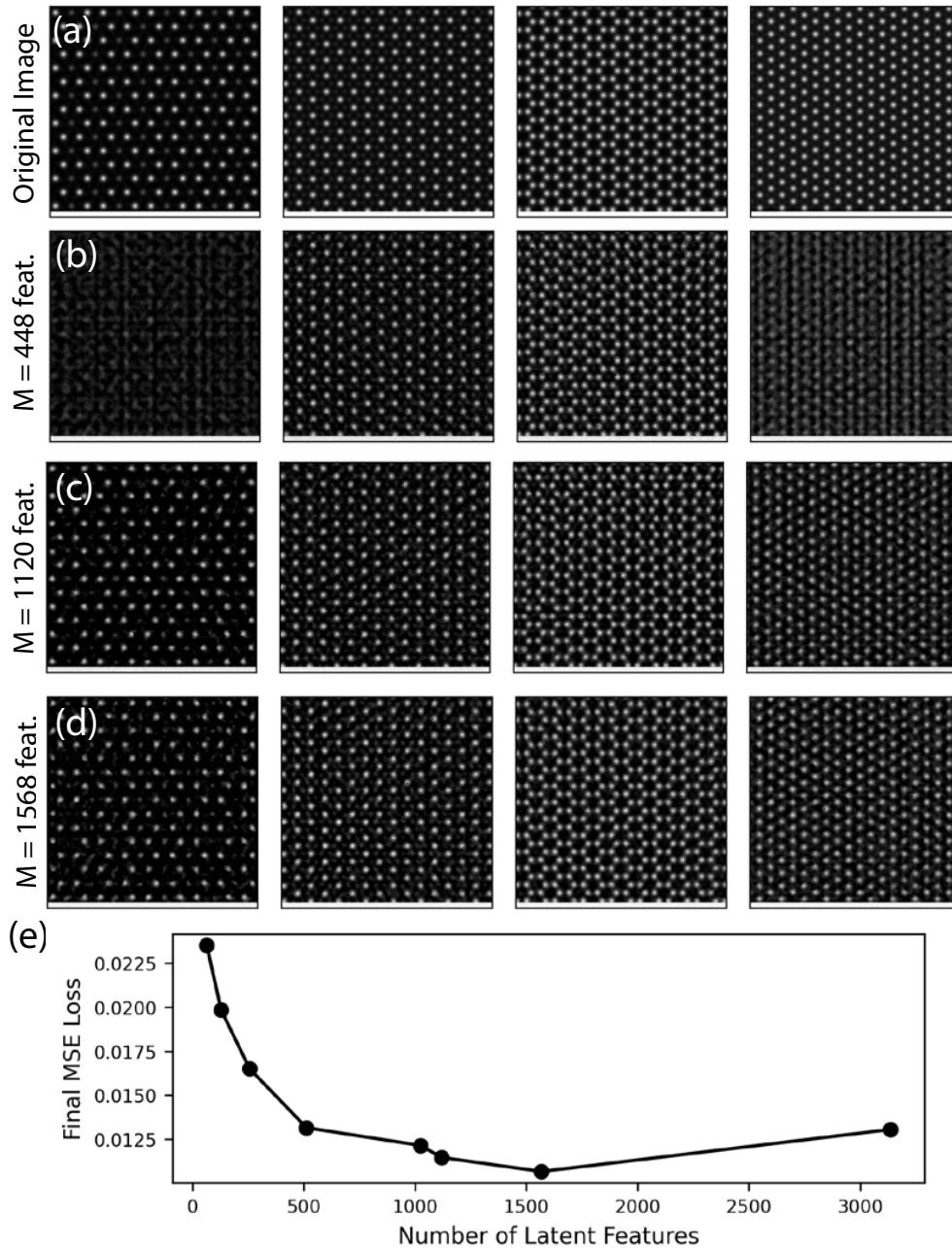


Figure 8: Autoencoder Reconstructed Images while varying the dimensionality of the latent space (M). Four randomly sampled images from the JARVIS-DFT-2D STEM database, corresponding to images of $\text{Tl}_2\text{SnAs}_2\text{S}_6$, CdCl_2 , Ba_2N , and NiH_2O_2 , are shown in row (a). Rows (b)-(d) show the images after reconstruction using autoencoder models, where three values for the latent dimensionality (M) are trialled: $M = 448$, 1120, or 1568. In panel (e), we show the final value of the MSE loss function after 200 training cycles (epochs) versus the number of latent features in the autoencoder model. Performance of the model, as determined by MSE loss as well as the visual quality of reconstructed images, improves when increasing from 448 to 1120 latent features, but does not significantly change when increasing to 1568 latent features. The MSE loss starts to increase at a larger number of latent features.

256x256 image, and use an auto-encoder of dimension 1120. In Fig. 8, we highlight the ability of the auto-encoders to reconstruct a few example images in the test dataset. We carried out AE training with dimensionalities of 64, 128, 256, 512, 1024, 1120, and 1568 features and an optimal value of 1568 was chosen. Moreover, the 1568 feature case visually appeared to yield reasonably reproduced images, while going to a larger number of latent features yielded a plateau in the quality of the reproduced images. Also, we note that the baseline loss (i.e. assuming an average of all the pixel values for the training set and using that average prediction on test set) is 77.006 which is much higher than the loss values we obtain. The reconstructed images bear a lot of similarity to the original images suggesting that the autoencoders developed in this work can be used for AE-related tasks such as dimensionality reduction.

Super-resolution GAN

The task of estimating a high-resolution (HR) image from its low-resolution (LR) counterpart is termed as super-resolution (SR).⁷⁰ SR is an active area of research in the field of computer vision. There have been several works in this field such as learned iterative shrinkage and thresholding algorithm (LISTA),⁷⁹ bicubic interpolation with CNN,⁸⁰ deeply-recursive convolutional network (DRCN),⁸¹ super-resolution variational autoencoder⁸² etc. However, such SR tasks are yet to be tackled in detail by the atomistic imaging community.^{5,31,32}

Here, we use a generative adversarial network (GAN) for enhancing the resolution of STEM images. We generate a dataset of 4-times low resolution (i.e., 64x64 instead of 256x256 size images) and using Super-Resolution Generative Adversarial Networks (SRGAN)⁷⁰ architecture, we develop a model to enhance resolution. A GAN model also has two components: namely generator, and discriminator. GAN's generator generates fake/synthetic data that could fool the discriminator. Its discriminator tries to distinguish fake data from real ones. This process is also termed as: min-max two-player game. Using the STEM image dataset, we train the generator-discriminator model and then generate high-resolution images in the

test set and show the results for one of the images in Fig.9. We note that unlike other neural networks, the losses in GANs can be counter-intuitive because the generator and discriminator are competing against each other. Nevertheless, we keep on training until we notice a plateau in the losses. Moreover, GAN’s performances can be viewed based on generated samples for which we show examples below. The low-resolution image is shown as LR while the high-resolution image is shown as HR. SRGAN uses VGG19 (visual geometry group convolutional neural network that is 19 layers deep)⁷¹ as feature extractor, however we notice that using shallow VGG19 feature extractor such as 4th layer (Fig. c) is equivalent to deeper layers such as Fig. d. Hence, a lower level feature extractor in VGG19 should be enough for resolution enhancement purposes. Note that though we demonstrate inverse design techniques such as auto-encoders and GANs in the present work, we plan to implement more advanced techniques such as variational auto-encoders,⁸³ stable-diffusion models⁸⁴ in the library as well soon.

Extracting images from arXiv dataset

Next, we use natural language processing with the open access arXiv dataset to curate datasets of STM and STEM images from the available literature. The arXiv dataset was previously used for ChemNLP project and has chemistry based information for the systems as well. We found more than 500 STM and 1500 STEM images from a simple search of STM, STEM in abstracts for the condensed-matter physics articles in arXiv. We further searched for such entries in the figure captions of the dataset and found more than 1000 such images that can be useful for image analytics. We show a few of the images obtained from the arXiv dataset in Fig.10. We provide the list of links to the images and corresponding papers in the AtomVision library.

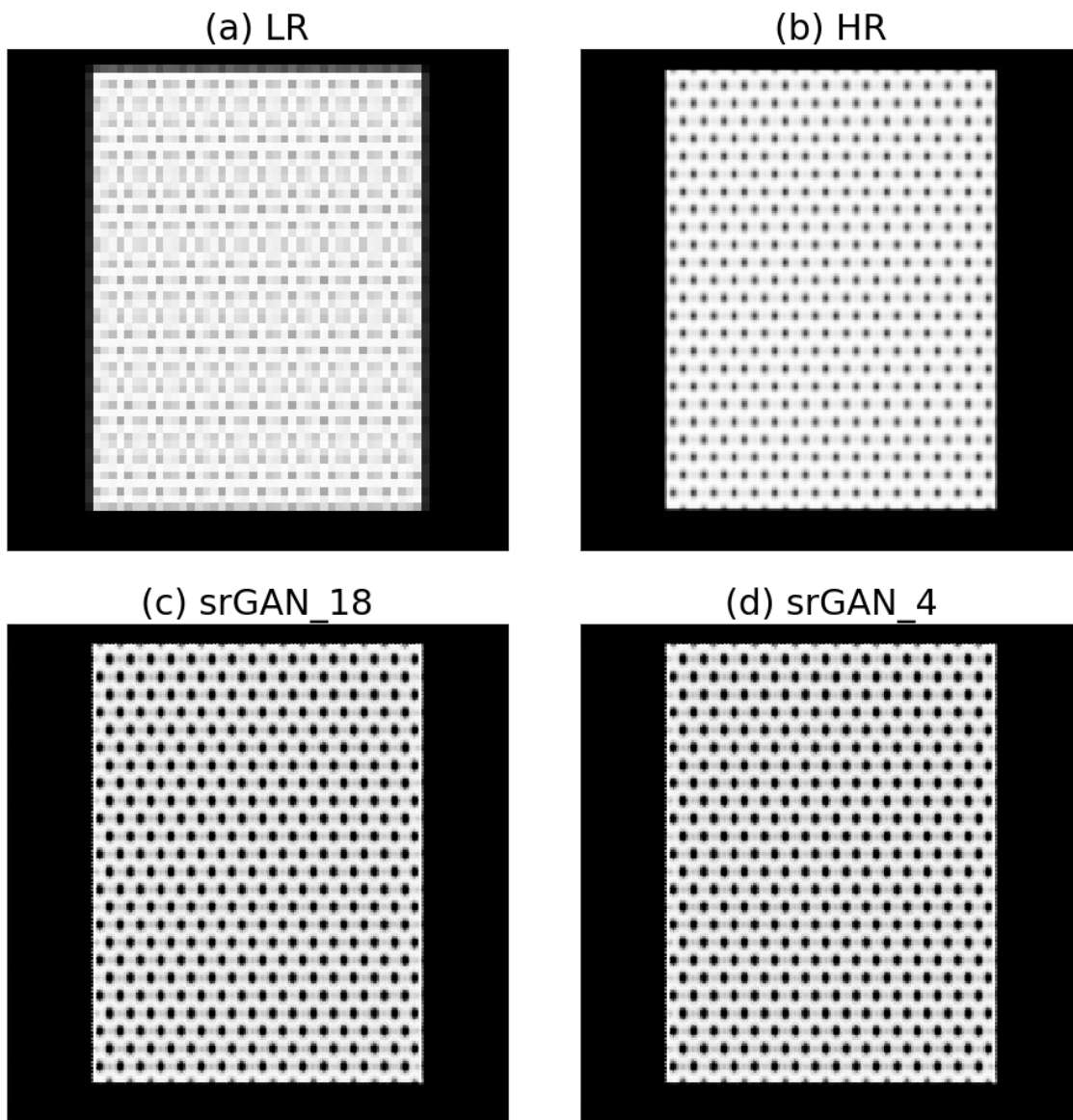


Figure 9: SR-GAN for enhancing image resolution. Examples for a) LR (low resolution), b) actual HR (high-resolution), c) SR-GAN VGG19’s 18th layer prediction, d) SR-GAN VGG19’s 4th layer prediction. We observe shallower layers of VGG19 gives similar predictions in terms of resolution enhancement as that of deeper layers.

Experimental image dataset

In addition to computational and NLP based microscopy image datasets, we also develop our own experimental image dataset in AtomVision. AtomVision provides a flexible and easy to use metadata capture template that can capture experimental set up across various mi-

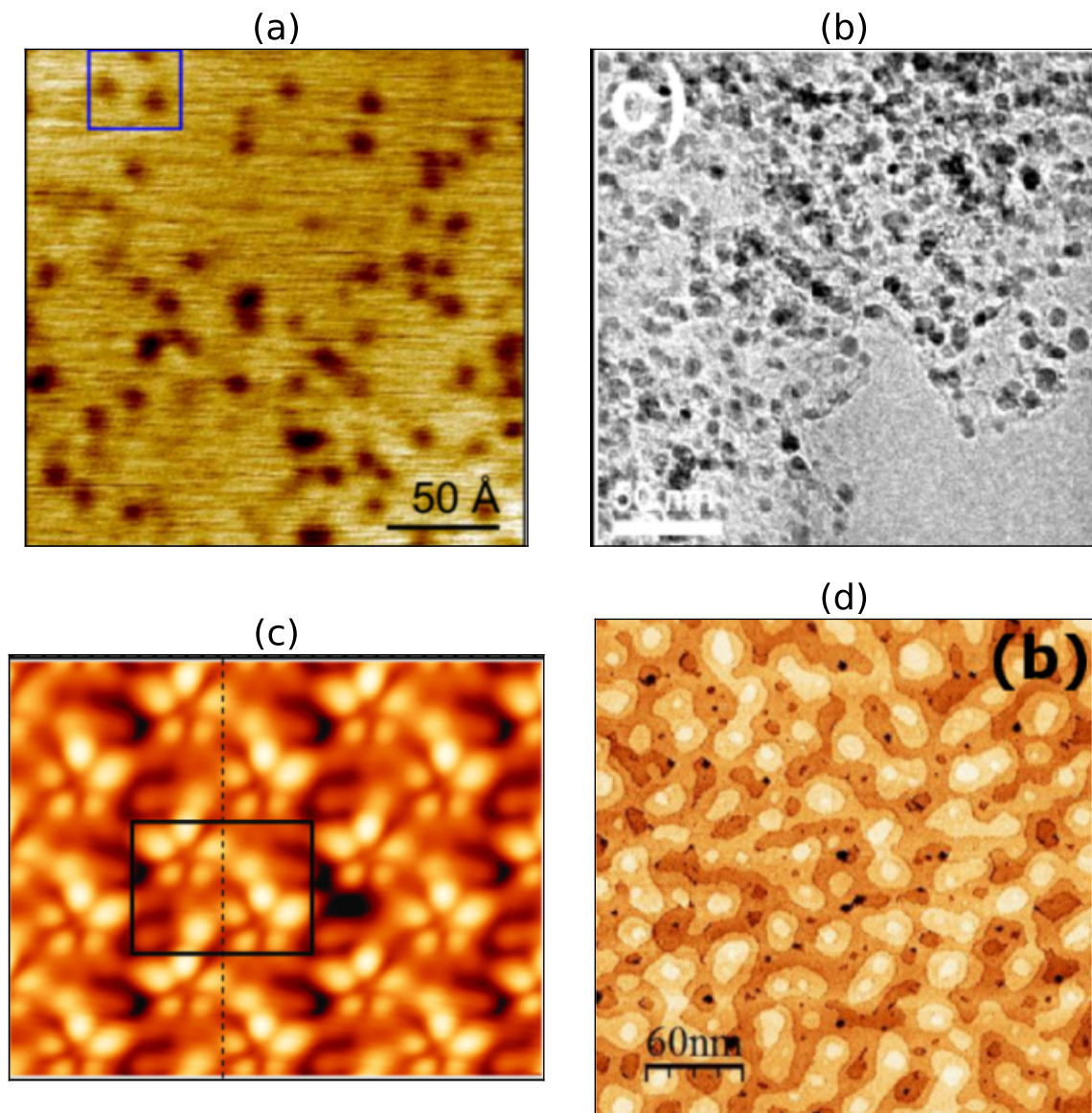


Figure 10: Example micrographs retrieved from the arXiv dataset. These figures are taken from: a) arXiv:0708.2306 for Dy,⁸⁵ b) arXiv:0805.3416 for $\text{FeC}_{32}\text{H}_{16}\text{N}_8$ ⁸⁶ c) arXiv:0807.3875 for Si⁸⁷ d) arXiv:0902.0626 for $\text{La}_{0.67}\text{Ca}_{0.33}\text{MnO}_3$.⁸⁸

croscopy instruments. This is motivated by previous works in this field such as refs.^{16,89} Such infrastructures provide frontend and backend meta-data capture schema and frameworks to capture and curate microscopy image data. Having an integrated framework for both experimental, computational and image based datasets in AtomVision will allow the investigation of several important challenges such as reproducibility, ground truth data and uncertainty in

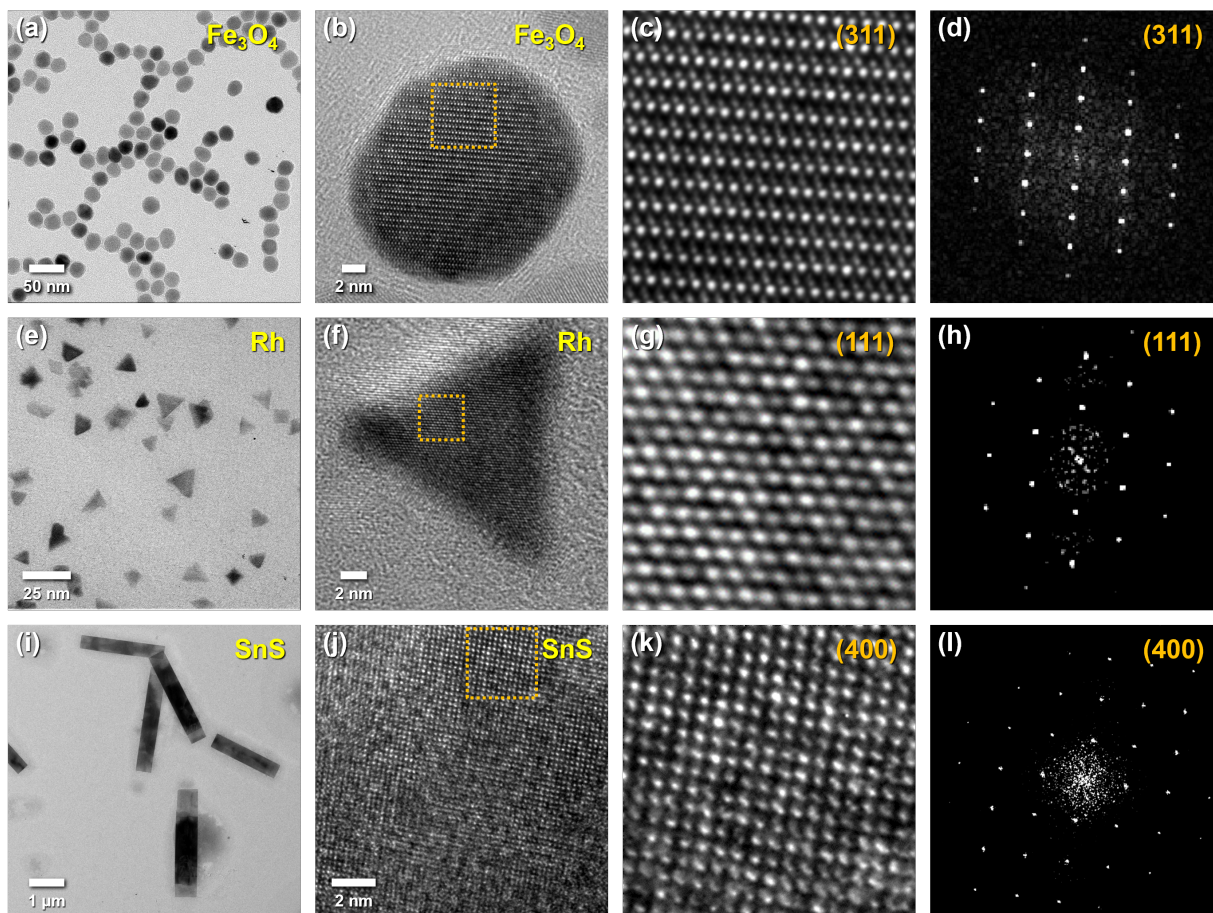


Figure 11: TEM and corresponding HRTEM images of solution-synthesized nanostructures. (a,b) Fe_3O_4 spherical nanoparticles, (e,f) Rh triangular nanoplates, and (i,j) SnS micron-sized nanoribbons. Regions of the HRTEM image indicated by dashed lines were magnified and analyzed by fast Fourier transform revealing crystallographic assignments of (c,d) Fe_3O_4 (311), (g,h) Rh (111), and α -SnS (400).

measurements. We show a few examples of TEM image dataset of nanoparticles in Fig.11. These nanoparticles TEM images are labelled by their different facet orientations leading to huge variability in the dataset for the same material. Currently, the experimental image dataset contains a few hundred of TEM images for various materials and their facets including Pt, Pd, Rh, Au, Fe_2O_3 , SnS etc. and we plan to continuously grow the dataset. We can integrate the AtomVision framework with NIST's and other microscopy measurement labs in the future to leverage several tools and datasets available in the library.

Conclusion

In summary, we have developed an integrated and general-purpose machine-vision library, especially for atomistic images. The dataset in AtomVision consists of both computational, experimental and literature based images providing a wide variety for general applications including machine/deep learning applications. The dataset mainly consists of scanning tunneling microscopy (STM) and scanning transmission electron microscopy (STEM) images and the framework would allow other atomic image datasets as well. There are numerous image machine learning techniques and we demonstrated applications of a few of them including convolution neural network, graph neural network, fully convolution neural network, generative adversarial network etc. Especially, the application of graph neural network such as ALIGNN on atomistic images provide a new paradigm for atomistic image analysis. The well-curated image dataset from experiments as well as the computational images can serve as a reference for many scientific applications.

Data availability statement

The data that support the findings of this study are openly available at the following URLs: <https://github.com/usnistgov/atomvision> and <https://doi.org/10.6084/m9.figshare.16788268>.

Acknowledgments

We thank the National Institute of Standards and Technology for funding, computational, and data-management resources. K.C. thanks the computational support from Extreme Science and Engineering Discovery Environment (XSEDE) computational resources under allocation number TG-DMR 190095. Contributions from K.C. were supported by the financial assistance award 70NANB19H117 from the U.S. Department of Commerce, National

References

- (1) Goodhew, P. J.; Humphreys, J.; Beanland, R. *Electron microscopy and analysis*; CRC press, 2000.
- (2) Krizhevsky, A.; Sutskever, I.; Hinton, G. E. Imagenet classification with deep convolutional neural networks. *Communications of the ACM* **2017**, *60*, 84–90.
- (3) Taigman, Y.; Yang, M.; Ranzato, M.; Wolf, L. Deepface: Closing the gap to human-level performance in face verification. Proceedings of the IEEE conference on computer vision and pattern recognition. 2014; pp 1701–1708.
- (4) Holm, E. A.; Cohn, R.; Gao, N.; Kitahara, A. R.; Matson, T. P.; Lei, B.; Yarasi, S. R. Overview: Computer vision and machine learning for microstructural characterization and analysis. *Metallurgical and Materials Transactions A* **2020**, *51*, 5985–5999.
- (5) Choudhary, K.; DeCost, B.; Chen, C.; Jain, A.; Tavazza, F.; Cohn, R.; Park, C. W.; Choudhary, A.; Agrawal, A.; Billinge, S. J.; Holm, E.; Ong, S. P.; Wolverton, C. Recent advances and applications of deep learning methods in materials science. *npj Computational Materials* **2022**, *8*, 1–26.
- (6) Vasudevan, R. K.; Choudhary, K.; Mehta, A.; Smith, R.; Kusne, G.; Tavazza, F.; Vlcek, L.; Ziatdinov, M.; Kalinin, S. V.; Hattrick-Simpers, J. Materials science in the artificial intelligence age: high-throughput library generation, machine learning, and a pathway from correlations to the underpinning physics. *MRS communications* **2019**, *9*, 821–838.
- (7) Modarres, M. H.; Aversa, R.; Cozzini, S.; Ciancio, R.; Leto, A.; Brandino, G. P. Neu-

- ral network for nanoscience scanning electron microscope image recognition. *Scientific reports* **2017**, *7*, 1–12.
- (8) Ge, M.; Su, F.; Zhao, Z.; Su, D. Deep learning analysis on microscopic imaging in materials science. *Materials Today Nano* **2020**, *11*, 100087.
- (9) Larmuseau, M.; Sluydts, M.; Theuwissen, K.; Duprez, L.; Dhaene, T.; Cottenier, S. Compact representations of microstructure images using triplet networks. *npj Computational Materials* **2020**, *6*, 1–11.
- (10) Yang, Z.; Li, X.; Catherine Brinson, L.; Choudhary, A. N.; Chen, W.; Agrawal, A. Microstructural materials design via deep adversarial learning methodology. *Journal of Mechanical Design* **2018**, *140*.
- (11) Hsu, T.; Epting, W. K.; Kim, H.; Abernathy, H. W.; Hackett, G. A.; Rollett, A. D.; Salvador, P. A.; Holm, E. A. Microstructure generation via generative adversarial network for heterogeneous, topologically complex 3d materials. *JOM* **2021**, *73*, 90–102.
- (12) Chun, S.; Roy, S.; Nguyen, Y. T.; Choi, J. B.; Udaykumar, H.; Baek, S. S. Deep learning for synthetic microstructure generation in a materials-by-design framework for heterogeneous energetic materials. *Scientific reports* **2020**, *10*, 1–15.
- (13) Dai, M.; Demirel, M. F.; Liang, Y.; Hu, J.-M. Graph neural networks for an accurate and interpretable prediction of the properties of polycrystalline materials. *npj Computational Materials* **2021**, *7*, 1–9.
- (14) Stan, T.; Thompson, Z. T.; Voorhees, P. W. Optimizing convolutional neural networks to perform semantic segmentation on large materials imaging datasets: X-ray tomography and serial sectioning. *Materials Characterization* **2020**, *160*, 110119.
- (15) Cohn, R.; Anderson, I.; Prost, T.; Tiarks, J.; White, E.; Holm, E. Instance segmentation

- for direct measurements of satellites in metal powders and automated microstructural characterization from image data. *JOM* **2021**, *73*, 2159–2172.
- (16) Taillon, J. A.; Bina, T. F.; Plante, R. L.; Newrock, M. W.; Greene, G. R.; Lau, J. W. NexusLIMS: A laboratory information management system for shared-use electron microscopy facilities. *Microscopy and Microanalysis* **2021**, *27*, 511–527.
- (17) DeCost, B. L.; Hecht, M. D.; Francis, T.; Webler, B. A.; Picard, Y. N.; Holm, E. A. UHCSDB: ultrahigh carbon steel micrograph database. *Integrating Materials and Manufacturing Innovation* **2017**, *6*, 197–205.
- (18) Jesse, S.; Chi, M.; Belianinov, A.; Beekman, C.; Kalinin, S.; Borisevich, A.; Lupini, A. Big data analytics for scanning transmission electron microscopy ptychography. *Scientific reports* **2016**, *6*, 1–8.
- (19) Schroff, F.; Criminisi, A.; Zisserman, A. Harvesting image databases from the web. *IEEE transactions on pattern analysis and machine intelligence* **2010**, *33*, 754–766.
- (20) Hua, X.-S.; Li, J. Prajna: Towards recognizing whatever you want from images without image labeling. Twenty-Ninth AAAI Conference on Artificial Intelligence. 2015.
- (21) Ziletti, A.; Kumar, D.; Scheffler, M.; Ghiringhelli, L. M. Insightful classification of crystal structures using deep learning. *Nature communications* **2018**, *9*, 1–10.
- (22) Choudhary, K.; Garrity, K. F.; Camp, C.; Kalinin, S. V.; Vasudevan, R.; Ziatdinov, M.; Tavazza, F. Computational scanning tunneling microscope image database. *Scientific data* **2021**, *8*, 1–9.
- (23) Schwenker, E.; Jiang, W.; Spreadbury, T.; Ferrier, N.; Cossairt, O.; Chan, M. K. EXSCLAIM!—An automated pipeline for the construction of labeled materials imaging datasets from literature. *arXiv preprint arXiv:2103.10631* **2021**,

- (24) Madsen, J.; Liu, P.; Kling, J.; Wagner, J. B.; Hansen, T. W.; Winther, O.; Schiøtz, J. A deep learning approach to identify local structures in atomic-resolution transmission electron microscopy images. *Advanced Theory and Simulations* **2018**, *1*, 1800037.
- (25) Maksov, A.; Dyck, O.; Wang, K.; Xiao, K.; Geohegan, D. B.; Sumpter, B. G.; Vasudevan, R. K.; Jesse, S.; Kalinin, S. V.; Ziatdinov, M. Deep learning analysis of defect and phase evolution during electron beam-induced transformations in WS₂. *npj Computational Materials* **2019**, *5*, 1–8.
- (26) Yang, S.-H.; Choi, W.; Cho, B. W.; Agyapong-Fordjour, F. O.-T.; Park, S.; Yun, S. J.; Kim, H.-J.; Han, Y.-K.; Lee, Y. H.; Kim, K. K.; Kim, Y.-M. Deep Learning-Assisted Quantification of Atomic Dopants and Defects in 2D Materials. *Advanced Science* **2021**, *8*, 2101099.
- (27) Roberts, G.; Haile, S. Y.; Sainju, R.; Edwards, D. J.; Hutchinson, B.; Zhu, Y. Deep learning for semantic segmentation of defects in advanced STEM images of steels. *Scientific reports* **2019**, *9*, 1–12.
- (28) Vlcek, L.; Ziatdinov, M.; Maksov, A.; Tselev, A.; Baddorf, A. P.; Kalinin, S. V.; Vasudevan, R. K. Learning from imperfections: predicting structure and thermodynamics from atomic imaging of fluctuations. *ACS nano* **2019**, *13*, 718–727.
- (29) Ziatdinov, M.; Maksov, A.; Kalinin, S. V. Learning surface molecular structures via machine vision. *npj Computational Materials* **2017**, *3*, 1–9.
- (30) Ovchinnikov, O. S.; O’Hara, A.; Jesse, S.; Hudak, B. M.; Yang, S.-Z.; Lupini, A. R.; Chisholm, M. F.; Zhou, W.; Kalinin, S. V.; Borisevich, A. Y.; Pantelides, S. T. Detection of defects in atomic-resolution images of materials using cycle analysis. *Advanced Structural and Chemical Imaging* **2020**, *6*, 1–9.
- (31) de Haan, K.; Ballard, Z. S.; Rivenson, Y.; Wu, Y.; Ozcan, A. Resolution enhancement in scanning electron microscopy using deep learning. *Scientific reports* **2019**, *9*, 1–7.

- (32) Ede, J. M.; Beanland, R. Partial scanning transmission electron microscopy with deep learning. *Scientific reports* **2020**, *10*, 1–10.
- (33) Rashidi, M.; Wolkow, R. A. Autonomous scanning probe microscopy in situ tip conditioning through machine learning. *Acs Nano* **2018**, *12*, 5185–5189.
- (34) Eppel, S.; Xu, H.; Bismuth, M.; Aspuru-Guzik, A. Computer vision for recognition of materials and vessels in chemistry lab settings and the vector-LabPics data set. *ACS central science* **2020**, *6*, 1743–1752.
- (35) Scime, L.; Siddel, D.; Baird, S.; Paquit, V. Layer-wise anomaly detection and classification for powder bed additive manufacturing processes: A machine-agnostic algorithm for real-time pixel-wise semantic segmentation. *Additive Manufacturing* **2020**, *36*, 101453.
- (36) Agrawal, A.; Choudhary, A. Deep materials informatics: Applications of deep learning in materials science. *Mrs Communications* **2019**, *9*, 779–792.
- (37) Bardeen, J. Tunnelling from a many-particle point of view. *Physical review letters* **1961**, *6*, 57.
- (38) Tersoff, J.; Hamann, D. R. Theory and application for the scanning tunneling microscope. *Physical review letters* **1983**, *50*, 1998.
- (39) Chen, C. J.; Smith, W. F. Introduction to scanning tunneling microscopy. *American Journal of Physics* **1994**, *62*, 573–574.
- (40) Combs, A. H.; Maldonis, J. J.; Feng, J.; Xu, Z.; Voyles, P. M.; Morgan, D. Fast approximate STEM image simulations from a machine learning model. *Advanced Structural and Chemical Imaging* **2019**, *5*, 1–10.
- (41) Kirkland, E. J. *Advanced computing in electron microscopy*; Springer, 1998; Vol. 12.

- (42) Kirkland, E. J. Computation in electron microscopy. *Acta Crystallographica Section A: Foundations and Advances* **2016**, *72*, 1–27.
- (43) Allen, L.; Findlay, S.; Oxley, M.; Rossouw, C. Lattice-resolution contrast from a focused coherent electron probe. Part I. *Ultramicroscopy* **2003**, *96*, 47–63.
- (44) Cowley, J.; Moodie, A. Fourier images: I-the point source. *Proceedings of the Physical Society. Section B* **1957**, *70*, 486.
- (45) Madsen, J.; Susi, T. The abTEM code: transmission electron microscopy from first principles. *Open Research Europe* **2021**, *1*, 24.
- (46) Ziatdinov, M.; Ghosh, A.; Wong, T.; Kalinin, S. V. AtomAI: a deep learning framework for analysis of image and spectroscopy data in (Scanning) transmission electron microscopy and beyond. *arXiv preprint arXiv:2105.07485* **2021**,
- (47) Somnath, S.; Smith, C. R.; Jesse, S.; Laanait, N. Pycroscopy-An Open Source Approach to Microscopy and Microanalysis in the Age of Big Data and Open Science. *Microscopy and Microanalysis* **2017**, *23*, 224–225.
- (48) Ophus, C. A fast image simulation algorithm for scanning transmission electron microscopy. *Advanced structural and chemical imaging* **2017**, *3*, 1–11.
- (49) Koch, C. T. *Determination of core structure periodicity and point defect density along dislocations*; Arizona State University, 2002.
- (50) Zhu, L.; Tang, J.; Li, B.; Hou, T.; Zhu, Y.; Zhou, J.; Wang, Z.; Zhu, X.; Yao, Z.; Cui, X.; Watanabe, K.; Taniguchi, T.; Li, Y.; Han, Z. V.; Zhou, W.; Huang, Y.; Liu, Z.; Hone, J. C.; Hao, Y. Artificial neuron networks enabled identification and characterizations of 2D materials and van der Waals Heterostructures. *ACS nano* **2022**, *16*, 2721–2729.

- (51) Moeck, P.; DeStefano, P. Accurate lattice parameters from 2D-periodic images for subsequent Bravais lattice type assignments. *Advanced Structural and Chemical Imaging* **2018**, *4*, 1–33.
- (52) Choudhary, K.; Garrity, K. F.; Reid, A. C. E.; DeCost, B.; Biacchi, A. J.; Hight Walker, A. R.; Trautt, Z.; Hattrick-Simpers, J.; Kusne, A. G.; Centrone, A.; Davydov, A.; Jiang, J.; Pachter, R.; Cheon, G.; Reed, E.; Agrawal, A.; Qian, X.; Sharma, V.; Zhuang, H.; Kalinin, S. V.; Sumpter, B. G.; Pilania, G.; Acar, P.; Mandal, S.; Haule, K.; Vanderbilt, D.; Rabe, K.; Tavazza, F. The joint automated repository for various integrated simulations (JARVIS) for data-driven materials design. *npj Computational Materials* **2020**, *6*, 1–13.
- (53) Choudhary, K.; DeCost, B. Atomistic Line Graph Neural Network for improved materials property predictions. *npj Computational Materials* **2021**, *7*, 1–8.
- (54) Kresse, G.; Furthmüller, J. Efficiency of ab-initio total energy calculations for metals and semiconductors using a plane-wave basis set. *Computational materials science* **1996**, *6*, 15–50.
- (55) Kresse, G.; Furthmüller, J. Efficient iterative schemes for ab initio total-energy calculations using a plane-wave basis set. *Phys. Rev. B* **1996**, *54*, 11169.
- (56) Yamashita, S.; Kikkawa, J.; Yanagisawa, K.; Nagai, T.; Ishizuka, K.; Kimoto, K. Atomic number dependence of Z contrast in scanning transmission electron microscopy. *Scientific reports* **2018**, *8*, 1–7.
- (57) Choudhary, K.; Kalish, I.; Beams, R.; Tavazza, F. High-throughput identification and characterization of two-dimensional materials using density functional theory. *Scientific Reports* **2017**, *7*, 1–16.
- (58) Hastrup, S.; Strange, M.; Pandey, M.; Deilmann, T.; Schmidt, P. S.; Hinsche, N. F.; Gjerding, M. N.; Torelli, D.; Larsen, P. M.; Riis-Jensen, A. C.; Gath, J.; Jacob-

- sen, K. W.; Mortensen, J. J.; Olsen, T.; Thygesen, K. S. The Computational 2D Materials Database: high-throughput modeling and discovery of atomically thin crystals. *2D Materials* **2018**, *5*, 042002.
- (59) Zhou, J.; Shen, L.; Costa, M. D.; Persson, K. A.; Ong, S. P.; Huck, P.; Lu, Y.; Ma, X.; Chen, Y.; Tang, H.; Feng, Y. P. 2DMatPedia, an open computational database of two-dimensional materials from top-down and bottom-up approaches. *Scientific data* **2019**, *6*, 1–10.
- (60) Choudhary, K.; Kelley, M. L. ChemNLP: A Natural Language Processing based Library for Materials Chemistry Text Data. *arXiv preprint arXiv:2209.08203* **2022**,
- (61) Biacchi, A. J.; Johnson, L. M.; Sweet, A. B.; Barrante, L. J.; Cal, E. M.; Hight Walker, A. R.; Buck, M. R. Polyoxovanadates as Precursors for the Synthesis of Colloidal Multi-Metal Oxide Nanocrystals. *Chemistry of Materials* **2022**, *34*, 2907–2918.
- (62) Biacchi, A. J.; Schaak, R. E. Ligand-induced fate of embryonic species in the shape-controlled synthesis of rhodium nanoparticles. *ACS nano* **2015**, *9*, 1707–1720.
- (63) Biacchi, A. J.; Le, S. T.; Alberding, B. G.; Hagmann, J. A.; Pookpanratana, S. J.; Heilweil, E. J.; Richter, C. A.; Hight Walker, A. R. Contact and Noncontact Measurement of Electronic Transport in Individual 2D SnS Colloidal Semiconductor Nanocrystals. *ACS nano* **2018**, *12*, 10045–10060.
- (64) Pedregosa, F.; Varoquaux, G.; Gramfort, A.; Michel, V.; Thirion, B.; Grisel, O.; Blondel, M.; Müller, A.; Nothman, J.; Louppe, G.; Prettenhofer, P.; Weiss, R.; Dubourg, V.; Vanderplas, J.; Passos, A.; Cournapeau, D.; Brucher, M.; Perrot, M.; Duchesnay, E. Scikit-learn: Machine learning in Python. *the Journal of machine Learning research* **2011**, *12*, 2825–2830.

- (65) Iakubovskii, P. Segmentation Models Pytorch. https://github.com/qubvel/segmentation_models.pytorch, 2019.
- (66) Ronneberger, O.; Fischer, P.; Brox, T. U-net: Convolutional networks for biomedical image segmentation. International Conference on Medical image computing and computer-assisted intervention. 2015; pp 234–241.
- (67) Huang, G.; Liu, Z.; Van Der Maaten, L.; Weinberger, K. Q. Densely connected convolutional networks. Proceedings of the IEEE conference on computer vision and pattern recognition. 2017; pp 4700–4708.
- (68) Paszke, A.; Gross, S.; Massa, F.; Lerer, A.; Bradbury, J.; Chanan, G.; Killeen, T.; Lin, Z.; Gimelshein, N.; Antiga, L.; Desmaison, A.; Köpf, A.; Yang, E.; DeVito, Z.; Raison, M.; Tejani, A.; Chilamkurthy, S.; Steiner, B.; Fang, L.; Bai, J.; Chintala, S. Pytorch: An imperative style, high-performance deep learning library. *Advances in neural information processing systems* **2019**, *32*.
- (69) Wang, M.; Zheng, D.; Ye, Z.; Gan, Q.; Li, M.; Song, X.; Zhou, J.; Ma, C.; Yu, L.; Gai, Y.; Xiao, T.; He, T.; Karypis, G.; Li, J.; Zhang, Z. Deep graph library: A graph-centric, highly-performant package for graph neural networks. *arXiv preprint arXiv:1909.01315* **2019**,
- (70) Ledig, C.; Theis, L.; Huszár, F.; Caballero, J.; Cunningham, A.; Acosta, A.; Aitken, A.; Tejani, A.; Totz, J.; Wang, Z.; Shi, W. Photo-realistic single image super-resolution using a generative adversarial network. Proceedings of the IEEE conference on computer vision and pattern recognition. 2017; pp 4681–4690.
- (71) Simonyan, K.; Zisserman, A. Very deep convolutional networks for large-scale image recognition. *arXiv preprint arXiv:1409.1556* **2014**,
- (72) Li, G.; Luican, A.; Andrei, E. Y. Scanning tunneling spectroscopy of graphene on graphite. *Physical review letters* **2009**, *102*, 176804.

- (73) O’Leary, C. M.; Haas, B.; Koch, C. T.; Nellist, P. D.; Jones, L. Increasing spatial fidelity and SNR of 4D-STEM using multi-frame data fusion. *Microscopy and Microanalysis* **2022**, *28*, 1417–1427.
- (74) Watashige, T.; Tsutsumi, Y.; Hanaguri, T.; Kohsaka, Y.; Kasahara, S.; Furusaki, A.; Sigrist, M.; Meingast, C.; Wolf, T.; Löhneysen, H. v., et al. Evidence for time-reversal symmetry breaking of the superconducting state near twin-boundary interfaces in FeSe revealed by scanning tunneling spectroscopy. *Physical Review X* **2015**, *5*, 031022.
- (75) Kang, L.; Ye, C.; Zhao, X.; Zhou, X.; Hu, J.; Li, Q.; Liu, D.; Das, C. M.; Yang, J.; Hu, D.; Chen, J.; Cao, X.; Zhang, Y.; Xu, M.; Di, J.; Tian, D.; Song, P.; Kutty, G.; Zeng, Q.; Fu, Q.; Deng, Y.; Zhou, J.; Ariando, A.; Miao, F.; Hong, G.; Huang, Y.; Pennycook, S. J.; Yong, K.-T.; Ji, W.; Wang, X. R.; Liu, Z. Phase-controllable growth of ultrathin 2D magnetic FeTe crystals. *Nature communications* **2020**, *11*, 1–9.
- (76) Mills, A.; Yu, Y.; Chen, C.; Huang, B.; Cao, L.; Tao, C. Ripples near edge terminals in MoS₂ few layers and pyramid nanostructures. *Applied Physics Letters* **2016**, *108*, 081601.
- (77) Dileep, K.; Sahu, R.; Sarkar, S.; Peter, S. C.; Datta, R. Layer specific optical band gap measurement at nanoscale in MoS₂ and ReS₂ van der Waals compounds by high resolution electron energy loss spectroscopy. *Journal of Applied Physics* **2016**, *119*, 114309.
- (78) Van der Walt, S.; Schönberger, J. L.; Nunez-Iglesias, J.; Boulogne, F.; Warner, J. D.; Yager, N.; Gouillart, E.; Yu, T. scikit-image: image processing in Python. *PeerJ* **2014**, *2*, e453.
- (79) Gregor, K.; LeCun, Y. Learning fast approximations of sparse coding. Proceedings of the 27th international conference on international conference on machine learning. 2010; pp 399–406.

- (80) Dong, C.; Loy, C. C.; He, K.; Tang, X. Learning a deep convolutional network for image super-resolution. *Computer Vision–ECCV 2014: 13th European Conference, Zurich, Switzerland, September 6-12, 2014, Proceedings, Part IV* 13. 2014; pp 184–199.
- (81) Kim, J.; Lee, J. K.; Lee, K. M. Deeply-recursive convolutional network for image super-resolution. *Proceedings of the IEEE conference on computer vision and pattern recognition*. 2016; pp 1637–1645.
- (82) Heydari, A. A.; Mehmood, A. SRVAE: super resolution using variational autoencoders. *Pattern Recognition and Tracking XXXI*. 2020; pp 87–100.
- (83) Kingma, D. P.; Welling, M. Auto-encoding variational bayes. *arXiv preprint arXiv:1312.6114* **2013**,
- (84) Ho, J.; Jain, A.; Abbeel, P. Denoising diffusion probabilistic models. *Advances in Neural Information Processing Systems* **2020**, *33*, 6840–6851.
- (85) Wegner, D.; Bauer, A.; Kaindl, G. Effect of impurities on Tamm-like lanthanide-metal surface states. *Physical Review B* **2007**, *76*, 113410.
- (86) Klinke, C.; Kern, K. Iron nanoparticle formation in a metal–organic matrix: from ripening to gluttony. *Nanotechnology* **2007**, *18*, 215601.
- (87) Battaglia, C.; Gaal-Nagy, K.; Monney, C.; Didiot, C.; Schwier, E. F.; Garnier, M. G.; Onida, G.; Aebi, P. A new structural model for the Si (331)-(12x1) reconstruction. *arXiv preprint arXiv:0807.3875* **2008**,
- (88) Kelly, S.; Galli, F.; Komissarov, I.; Aarts, J. Correlations between the morphology and the electronic structure at the surface of thin film manganites, investigated with STM. *arXiv preprint arXiv:0902.0626* **2009**,
- (89) Nguyen, P.; Konstanty, S.; Nicholson, T.; O’Brien, T.; Schwartz-Duval, A.; Spila, T.; Nahrstedt, K.; Campbell, R. H.; Gupta, I.; Chan, M.; Mchenry, K.; Paquin, N. 4ceed:

Real-time data acquisition and analysis framework for material-related cyber-physical environments. 2017 17th IEEE/ACM International Symposium on Cluster, Cloud and Grid Computing (CCGRID). 2017; pp 11–20.

TOC graphic

